Observed Bulk Hook Echo Drop Size Distribution Evolution in Supercell Tornadogenesis and Tornadogenesis Failure

KRISTOFER S. TUFTEDAL,[a] MICHAEL M. FRENCH,[a] DARREL M. KINGFIELD,[b,c] AND JEFFREY C. SNYDER[d]

[a] *School of Marine and Atmospheric Science, Stony Brook University, Stony Brook, New York*
[b] *Cooperative Institute for Research in Environmental Sciences, University of Colorado Boulder, Boulder, Colorado*
[c] *NOAA/Global Systems Laboratory, Boulder, Colorado*
[d] *NOAA/OAR National Severe Storms Laboratory, Norman, Oklahoma*

(Manuscript received 28 October 2020, in final form 7 May 2021)

ABSTRACT: The time preceding supercell tornadogenesis and tornadogenesis "failure" has been studied extensively to identify differing attributes related to tornado production or lack thereof. Studies from the Verification of the Origins of Rotation in Tornadoes Experiment (VORTEX) found that air in the rear-flank downdraft (RFD) regions of non- and weakly tornadic supercells had different near-surface thermodynamic characteristics than that in strongly tornadic supercells. Subsequently, it was proposed that microphysical processes are likely to have an impact on the resulting thermodynamics of the near-surface RFD region. One way to view proxies to microphysical features, namely, drop size distributions (DSDs), is through use of polarimetric radar data. Studies from the second VORTEX used data from dual-polarization radars to provide evidence of different DSDs in the hook echoes of tornadic and nontornadic supercells. However, radar-based studies during these projects were limited to a small number of cases preventing result generalizations. This study compiles 68 tornadic and 62 nontornadic supercells using Weather Surveillance Radar–1988 Doppler (WSR-88D) data to analyze changes in polarimetric radar variables leading up to, and at, tornadogenesis and tornadogenesis failure. Case types generally did not show notable hook echo differences in variables between sets, but did show spatial hook echo quadrant DSD differences. Consistent with past studies, differential radar reflectivity factor (Z_{DR}) generally decreased leading up to tornadogenesis and tornadogenesis failure; in both sets, estimated total number concentration increased during the same times. Relationships between DSDs and the near-storm environment, and implications of results for nowcasting tornadogenesis, also are discussed.

KEYWORDS: Tornadogenesis; Supercells; Tornadoes; Convective storms; Drop size distribution; Radars/Radar observations

1. Introduction

Despite major advances in our understanding of supercell tornadoes over the past two decades, skillful, short-term (0–1 h) forecasting (i.e., "nowcasting") of tornadogenesis remains elusive owing to a lack of understanding of the complicated processes involved and a dearth of observations at the spatiotemporal scales commensurate with the process. Work to distinguish differences between tornadic and nontornadic supercells are ongoing using both observations and numerical simulations (e.g., Davies-Jones and Brooks 1993; Brooks et al. 1994; Stensrud et al. 1997; Rasmussen and Blanchard 1998; Markowski et al. 2002; Grzych et al. 2007; Markowski et al. 2011; Parker 2014; Weiss et al. 2015; French et al. 2015; Klees et al. 2016; Coffer and Parker 2017, 2018). From this body of work, one known important contributor to tornadogenesis is the thermodynamic characteristics of the rear-flank downdraft (RFD) region, likely because some air parcels ingested by a supercell's updraft have been shown to pass through the RFD outflow region (e.g., Markowski et al. 2012), and enter the low-level mesocyclone (e.g., Brandes 1978; Lemon and Doswell 1979; Jensen et al. 1983; Markowski and Richardson 2009). The thermodynamic characteristics of these parcels may be an important factor in tornado production (Markowski et al. 2002; Grzych et al. 2007; Markowski et al. 2011; Markowski and Richardson 2014, 2017) because parcels that are less negatively buoyant may be more conducive to rising in the updraft and stretching vertical vorticity.

Vorticity generation in supercells is sensitive to the location and strength of the RFD. In simulated "pseudostorms," it was shown that, in environments with strong low-level shear, the baroclinic generation of the near-surface circulation was highly sensitive to the strength of the heat sink, a proxy for the RFD (Markowski and Richardson 2014). Heat sinks of intermediate strength, and therefore weak negative buoyancy, produced the strongest cyclonic vortex when compared to stronger and weaker heat sinks, where strong vortices failed to form. Model simulations of these pseudostorms showed that the development of near-surface vertical vorticity is highly sensitive to the location of the heat sink as well (Markowski and Richardson 2017). Therefore, both the location and buoyancy of RFD air may be critically important to tornado production.[1]

The RFD is driven by negative buoyancy, precipitation loading, and/or downward-directed vertical perturbation pressure gradient forces (Markowski 2002). Hydrometeors from the RFD that

Corresponding author: Kristofer S. Tuftedal, kristofer.tuftedal@stonybrook.edu

[1] The characteristics of the forward flank downdraft (FFD) region also may play an important, but undetermined role in vorticity generation and tornado production (e.g., Shabbott and Markowski 2006; Beck and Weiss 2013; Orf et al. 2017; Murdzek et al. 2020).

DOI: 10.1175/MWR-D-20-0353.1

populate the near-surface air contribute to the hook echo (e.g., Rasmussen et al. 2006) observed in radar reflectivity data. A potential microphysical control of the buoyancy of RFD outflow air is the evaporation rate of rain drops within the RFD region. The evaporation rate can affect the thermodynamic characteristics of the RFD outflow air and therefore its buoyancy (Markowski et al. 2002). For example, low evaporation rates would lead to less evaporative cooling within the RFD region and would allow for less negatively buoyant air to develop within RFD outflow, and vice versa. *Concurrently, evaporation impacts the rain drop sizes present in the hook echo of the supercell*. Evaporation tends to preferentially reduce the number concentration of the smallest drops [i.e., the smallest drops evaporate after falling a shorter distance compared to the larger drops; e.g., Li and Srivastava (2001)], in turn increasing the importance of the larger drops in defining the drop size distribution (DSD) (Kumjian 2011).

Finally, changes in median rain drop sizes owing to changes in the evaporation rates within the hook echo may be identified, in a bulk sense, by analyzing polarimetric weather radar data. One microphysical fingerprint is the DSD in the storm's hook echo, a proxy for the RFD outflow region. Supercell DSDs have been measured directly through use of disdrometers in a small set of studies (Schuur et al. 2001: Friedrich et al. 2013; Dawson et al. 2013; Kalina et al. 2014), but the lack of spatial coverage in each case belies DSD generalizations. Also, disdrometers are subject to damage from storm hazards and poor placement within the storm. An alternative is to use polarimetric radar bulk DSD retrieval, which can provide information about the entire storm, but relies on derived relationships between radar reflectivity factor at horizontal polarization (Z_H), differential radar reflectivity factor (Z_{DR}) (which is subject to biases), and observed drop sizes.

Crowe et al. (2012) used the Z_{DR} and specific differential phase (K_{DP}; a variable that is related to the total liquid water content) data of 20 storms (16 tornadic and four nontornadic) from the C-Band Advanced Radar for Meteorological and Operational Research (ARMOR) to investigate how dual-polarization fields varied across storm types. They showed that there was considerably more horizontal separation in the maxima of Z_{DR} and K_{DP} in tornadic cases than in nontornadic cases. The Z_{DR} was enhanced near and along the forward flank reflectivity gradient, and K_{DP} was enhanced left of the forward flank of the storm (in the forward flank) in tornadic (nontornadic) supercell cases. Little to no overlap in these maxima occurred in the tornadic cases whereas more substantial overlap occurred in the nontornadic cases, perhaps owing to differences in the concentrations of various drop sizes within various regions of these storms.

Loeffler et al. (2020) expanded on the previous study by investigating the horizontal separation characteristics of Z_{DR} and K_{DP} for 116 supercell cases (63 tornadic and 53 nontornadic) using data from the Weather Surveillance Radar–1988 Doppler (WSR-88D) network. They found significant differences between case types when analyzing the orientation of the separation of Z_{DR} and K_{DP} maxima with respect to storm motion. Tornadic (nontornadic) cases exhibited K_{DP}/Z_{DR} separation vector orientations that tended to be closer to 90° to the right of (parallel to) the storm motion. Separation vector orientations that are orthogonal to storm motion likely result from K_{DP} maxima that are farther from the updraft of the storm, which they speculated could aid in tornadogenesis by keeping the negatively buoyant air produced by areas with high precipitation content far from the updraft. However, in Loeffler and Kumjian (2020), the authors used a simple hydrometeor size sorting model to show that the orientation of the separation vector was related to the mean storm-relative winds, and that the orientation changed with increases in storm-relative helicity. Regardless of the exact cause, the results of these studies suggest that differences in K_{DP} exist between tornadic and nontornadic supercells.

Kumjian and Ryzhkov (2008), Kumjian (2011), and French et al. (2015) used polarimetric radar data to investigate the hook echo region of supercells by leveraging the relationship between bulk raindrop sizes and Z_{DR}. Since Z_{DR} is a proxy for the bulk raindrop size (owing to the relationship between drop size and shape), small bulk raindrop sizes are associated with lower Z_{DR}. Kumjian and Ryzhkov (2008) were the first to analyze polarimetric differences between tornadic (four) and nontornadic (five) supercells. At S-band, they found that tornadic supercells had lower Z_{DR} for a given Z_H in the hook echo than did the nontornadic cases, though there was substantial overlap in the Z_{DR} distributions (Fig. 1a). Kumjian (2011) analyzed six tornadic supercells with S- and C-band radar data and found that the hook echoes in those cases had anomalously high small drop concentrations, particularly in the left forward (LF) and right forward (RF) quadrants of the hook echo. The author hypothesized that warm rain processes brought small drops to the surface rapidly via dynamically forced downdrafts.

French et al. (2015) used X-band radar data to analyze 15 supercells, 6 tornadic and 9 nontornadic, from the second Verification of the Origins of Rotation in Tornadoes Experiment (VORTEX2; Wurman et al. 2012). They found, similar to Kumjian and Ryzhkov (2008), that the tornadic supercells exhibited generally lower Z_{DR} in the hook echo than nontornadic supercells. They also observed one case in which the mean Z_{DR} dropped and the percentage of radar gates characterized by small drops increased in the time *leading up to* tornadogenesis (Fig. 1b). The study also evaluated near-storm environments (NSEs) using VORTEX2 proximity soundings and found that cases with an abundance of small drops had lower lifting condensation levels (LCLs) and higher boundary layer relative humidity (RH) than the large drop cases. They proposed that lower LCLs and higher RHs lead to a decrease in evaporation rate in the hook echo. In turn, a reduction in evaporative cooling contributes to the production of less negatively buoyant vorticity rich air in the hook echo, which is more easily ingested by the supercell's updraft allowing for tilting and stretching of that vorticity during tornadogenesis. They argued further that reduced evaporation rates also help explain the long-known link between lower LCLs and tornado formation (Rasmussen and Blanchard 1998).

Given repeated observations of unusual DSD markers in supercell hook echoes, Kumjian et al. (2015) used an idealized simulation of a supercell to analyze the formation processes and associated DSDs for all regions of the supercell. Consistent

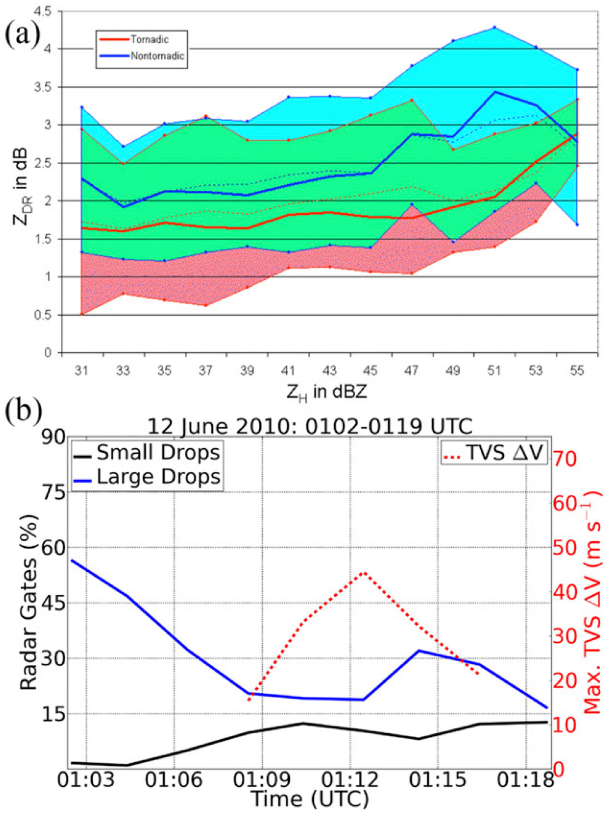

FIG. 1. (a) Comparison of Z_H and Z_{DR} for tornadic and nontornadic supercell hook echoes. The thick red (blue) lines denote the median Z_{DR} value for a given Z_H for tornadic (nontornadic) supercell hook echoes, and thin dashed red (blue) lines denote mean Z_{DR} for the same respective quantities. Thin solid lines denote ±1 standard deviation from their respective mean lines. The area shaded in green shows where the tornadic and nontornadic Z_{DR} values overlap, and the pink (aqua) shaded regions represent Z_{DR} values for only tornadic (nontornadic) hook echo values. From Kumjian and Ryzhkov (2008). (b) Time series showing the total percentage of radar gates characterized by small (black line) and large (blue line) drops during the life cycle of a tornado on 12 Jun 2010. The dotted red line in shows the approximate intensity (magnitude of the sum of maximum inbound and outbound radial velocities) of the tornadic vortex signature (TVS) associated with the tornado. From French et al. (2015).

with the observations made in Kumjian (2011), they found that, in the hook echo, anomalously small rain drops were formed from warm rain processes and brought to the surface through shallow downdrafts within the RFD. Warm rain processes were the dominant contributor to rain formation within the majority of the hook echo, though there were also small contributions from drops shed from hail above 0°C and from completely melted hail stones.

Though multiple observational studies now have hinted at different polarimetric characteristics in tornadic and nontornadic hook echoes, they are hindered by a low sample of cases (i.e., only 6–15 supercells in each study). In addition, Van Den Broeke (2020) recently found that "pretornadic" supercell hook echoes tended to have overall *larger* mean Z_{DR} than nontornadic supercells, though direct comparisons between tornadic and nontornadic cases were not made. Therefore, a climatological approach is needed to further examine potential bulk DSD differences between case types, to elucidate any microphysical hook echo differences between tornadic and nontornadic supercells, and determine the utility of any identified relationships for nowcasting.

This study presents a climatology of hook echo polarimetric and bulk DSD characteristics in 130 tornadic and nontornadic supercells observed by the polarimetric WSR-88D network. Strict case selection ensures low-level coverage and mitigates the impacts of storm mergers and other external contributors, and a rigorous Z_{DR} bias correction ensures data accuracy. This study is one in an ongoing series of climatological studies of polarimetric characteristics of supercells by the authors (French and Kingfield 2019; Loeffler et al. 2020), in addition to other recent studies (Homeyer et al. 2020). Section 2 outlines the process of case selection, data quality, and analysis methodology, section 3 presents the analysis of these observations, and section 4 discusses the results found herein with speculation on the physical causes of any apparent differences.

2. Data and methods

a. Case selection

To obtain the tornadic supercell data used for this study, we began with all recorded supercell tornadoes in the Storm Prediction Center (SPC) convective mode database between 2013 and 17 (Smith et al. 2012); the dual-polarization upgrade to the WSR-88D network was completed in 2013, and the most recent addition to the convective mode database was for 2017. From there, only cases that occurred within 60 km of a WSR-88D site at the estimated time of tornadogenesis and 20 min prior were considered. The range requirement allowed for radar data to be analyzed at 500 ± 150 m above ground level (AGL) at each time to approximate near-surface bulk DSDs. Each tornado case that met the range threshold was then manually examined. Any tornadoes that occurred within storms that underwent cyclic mesocyclogenesis prior to tornadogenesis and/or within storms where subsequent tornadoes spawned from cyclic tornadogenesis were excluded, as were any storms where the hook echo was not discrete, (i.e., no storm mergers). The additional requirements on case selection mitigated external storm effects on any observed DSD signal. Supercells which met the criteria were analyzed for 3–4 volume scans prior to, and at the time of, tornadogenesis. For some parts of this study, the enhanced Fujita scale (EF; Edwards et al. 2013) rating was used to divide cases into weakly (EF0–1) and strongly (EF2–4) tornadic cases for the investigation of potential differences in the hook echo DSDs of tornadoes of varying intensity.

To obtain the nontornadic supercell data used for this study, an SPC database of hazardous storms that occurred during 2015 was used. In the database, the mode of every storm that produced a severe hazard (tornado, hail, and wind) in the United States was logged. To choose nontornadic cases, we

mined the database for storms that were logged as supercells, but had no associated tornado report. As with the tornadic cases, nontornadic cases were required to be within 60 km of a WSR-88D site and have a discrete hook echo. The 0–1-km azimuthal shear (Mahalik et al. 2019) was manually analyzed in the nontornadic supercells. The time at which the maximum azimuthal shear occurred collocated with the velocity couplet was assumed to be its tornadogenesis failure scan. Tornadogenesis failure scans that only had an apparent velocity couplet at the time of tornadogenesis failure also were included for direct comparison with the tornadogenesis scans. Low-level rotation associated with a mesocyclone was not always apparent for the nontornadic cases, and so two subsets of *strongly* rotating nontornadic supercells were developed using two different thresholds. The first threshold required the 0–1-km azimuthal shear of nontornadic cases at the time of tornadogenesis failure ("F") to be greater than or equal to one standard deviation below the mean of the tornadic 0–1-km azimuthal shear one scan prior to tornadogenesis ("G-1"). The second threshold used the 25th percentile of the same tornadic azimuthal shear as the cutoff. These thresholds were then applied to the nontornadic dataset to test the sensitivity of the results herein to rotational intensity of nontornadic supercells. The G-1 time of azimuthal shear was used instead of the time of tornadogenesis ("G") to avoid contamination of the azimuthal shear by an ongoing tornado.

b. Hook echo isolation

Examination of all cases that met the detailed criteria was completed using Warning Decision Support System–Integrated Information (WDSS-II; Lakshmanan et al. 2007). Isolating the hook echoes allowed for the study to focus on the RFD region of storms, and was done subjectively by identifying the backend of the hook echo first, tracing it into the forward flank of the storm, and then terminating it where the approximate gradient in reflectivity width was maximized (e.g., French et al. 2015). The same process was followed for three to four WSR-88D volumes (~4–6 min per volume) prior to G or F. In more recent cases, Supplemental Adaptive Intravolume Low-level Scan (SAILS; Chrisman 2013) and Multiple Elevation Scan Option SAILS (MESO-SAILS; Chrisman 2014) scans were available. If a change in radar elevation angle was not necessary to keep the hook echo height within the 500 ± 150 m threshold for the duration of an event, the supplementary scan closest to the time of tornadogenesis or tornadogenesis failure was used. Successive SAILS or MESO-SAILS scans were not used to maintain consistency with non-SAILS cases.

Once the hook echo was isolated, a polygon was created that enclosed the hook echo (not shown). The data recorded at the vertices of the polygons included the approximate height above mean sea level (MSL) of the radar beam (later corrected to approximately AGL by subtracting the radar's height MSL), latitude, longitude, and radar scan time. Hook echoes were investigated at the elevation angle which allowed for the majority of the hook echo to be sampled at 500 ± 150 m AGL. Using the ~500-m height level allowed for sampling to occur as close to the surface as possible while maintaining a large sample of cases.

c. Relationship between Z_H, Z_{DR}, and derived quantities

In this study, DSDs are estimated by using $Z_{\rm H}$ and $Z_{\rm DR}$ comparisons as a proxy for raindrop size. The Z_H, and radar reflectivity factor at vertical polarization (Z_V), contains information about the power returned to the radar. The $Z_{\rm DR}$ contains information about drop shape by comparing the horizontal and vertical radar reflectivity; $Z_{\rm DR}$ generally is positive for oblate scatterers, near zero for spherical or large concentrations of randomly oriented tumbling scatterers, and negative for prolate scatterers. Using Z_H and $Z_{\rm DR}$, median drop size (D_0) can be estimated using (1), and total number concentration (N_T) estimated using (2), as obtained in Cao et al. (2008) via relations derived from video disdrometer data and radar data in Oklahoma:

$$D_0 = 0.0436Z_{\rm DR}^3 - 0.216Z_{\rm DR}^2 + 1.076Z_{\rm DR} + 0.659, \quad (1)$$

$$N_T = Z_H \times 10^{(-0.0837Z_{\rm DR}^3 + 0.702Z_{\rm DR}^2 - 2.062Z_{\rm DR} + 0.794)}. \quad (2)$$

The relationships in (1) and (2) allow analysis which may infer bulk microphysical processes that occur within a storm through the use of polarimetric radar data. The empirical relationships derived between radar variables and microphysical characteristics in Cao et al. (2008) were used in this study since they were obtained from convective thunderstorms and should be a reasonable approximation of the actual values found within supercells, though certainly not without error. In addition, because these empirical relationships were derived for convection in Oklahoma, there is likely to be regional variability in D_0 and N_T that this study does not account for.

d. Z_{DR} bias correction

Bulk DSD results are subject to the effects of $Z_{\rm DR}$ bias. For each case analyzed, the individual biases in $Z_{\rm DR}$ were estimated for each radar on the day that the case occurred by replicating the process used by the Radar Operations Center. The bias in $Z_{\rm DR}$ was calculated by using a weighted average of the bias estimates using three methods: light rain, dry snow, and Bragg scatter signatures. To retrieve the bias estimates, all volume scans ±48 h from the time of G or F were used. The weighted mean was calculated from the median biases of light rain, dry snow, and Bragg scatter signatures using weights of 0.25, 0.33, and 0.42, respectively (Richardson et al. 2017). Differential attenuation correction was not performed on these data.

The bias values were removed from the raw $Z_{\rm DR}$ data in order to recalculate variables derived from Cao et al. (2008) (Fig. 2). Individual radar $Z_{\rm DR}$ biases should not change an appreciable amount during a particular case (i.e., over a 20-min period), so these biases were considered constant for the duration of the analysis period. The use of a stringent bias correction technique allowed for a more accurate evaluation of bulk DSD changes.

e. Hook echo examination

Before calculated quantities were obtained, the data were thresholded by considering only those gates with copolar correlation coefficient ($\rho_{\rm hv}$) values of ≥0.97 in order to identify

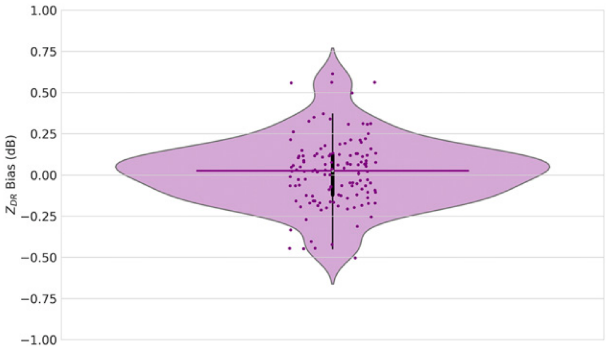

FIG. 2. Violin plot of the Z_{DR} biases for all 130 tornadic (68) and nontornadic cases (62). The thick, black vertical line denotes the interquartile range. The thin, black lines extending below and above the interquartile range extends to the 5th and 95th percentiles, respectively. The horizontal purple line denotes the median biases of all cases.

rain and mitigate any hail or nonmeteorological scatterer contamination, similar to Kumjian and Ryzhkov (2008) and French et al. (2015). Then, the empirical relationships described in Cao et al. [2008; Eqs. (1) and (2)] were used to calculate DSD characteristics for the hook echoes of each storm. The Z_{DR} data were subdivided into 5-dB Z_H bins, 30–35, 35–40, 40–45, and 45–50 dBZ because of the increasingly positive slope in Z_{DR} with increasing Z_H shown in Cao et al. (2008). The bulk Z_H, Z_{DR}, K_{DP}, D_0, and N_T for all cases were evaluated for each time step prior to G and F if the hook echo at that time step surpassed a 20-radar gate threshold. The K_{DP} was calculated from the differential phase shift (Φ_{DP}) using the WDSS-II algorithm "w2dualpol," which calculates K_{DP} at the same spatial resolution as the WSR-88D Radar Product Generator system used operationally by the National Weather Service.

For analysis, the median values of a given variable were taken from all thresholded gates contained within the hook echo polygon for that time. The median values were extracted at all available times for all cases and then sorted based on their case types. The values were also used to find the change in a given variable using

$$\Delta x_{\text{norm}} = \frac{[x(t) - x(t-1)]\Delta s_{\text{norm}}}{\Delta s_{\text{actual}}}, \tag{3}$$

where Δx_{norm} is the linearly time-normalized change in a given variable, $x(t)$ is the value of a given variable at the current time, $x(t-1)$ is the value of the same variable at one time step previous, Δs_{norm} is the normalization time of 300 s to linearly adjust values, and Δs_{actual} is the actual time between scans in seconds. The time between radar scans varied by a minute or more depending on the volume coverage pattern (VCP) the radar was using, so normalizing to one duration between scans allowed for the change in a variable to be better related to a physical process, rather than discrepancies in the time between scans. As a result, scans prior to G/F represent a range in times rather than exact times prior to each event. The maximum time between scans for the tornadic (nontornadic) cases presented in this study is 478 (560) seconds, the median time between scans is 308 (311) seconds, and the interquartile range of time between scans is 44 (31) seconds.

Hook echoes were subdivided into four quadrants for drop size spatial analysis: LF, RF, left backward (LB), and right backward (RB). The abscissa dividing the hook echoes into left and right quadrants were determined using a given storm's mean motion as determined by tracking the centroid of the hook echo polygon over time. The ordinate dividing the hook echoes into forward and back quadrants were determined by the centroid of the hook echo polygon at the time of tornadogenesis.

f. Near-storm environment analysis

The NSE of cases was analyzed to determine the relationship between LCLs and small drops and also determine any potential relationships between drop size, storm relative helicity (SRH), and shear vector magnitude. The NSE was estimated using Rapid Refresh model (RAP; Benjamin et al. 2016) data in a subset of cases where the surrounding environment was not convectively contaminated. The LCL, 0–1-km SRH, and 0–1-km shear vector magnitude from the grid point closest to the storm, and within its inflow region based on its apparent motion and boundary layer winds, were recorded. The time of the fourth scan (or third scan if a fourth did not exist) prior to G and F was used to determine the RAP analysis time, which always occurred prior to that scan's time.

g. Statistical analysis

To assess any statistically significant differences between given variables for case types at the time of G and F, the nonparametric Mann–Whitney U test was used (Mann and Whitney 1947). Further, to assess any statistically significant changes in given variables during the time leading up to G and F, another nonparametric test, the Wilcoxon signed-rank test, was used (Wilcoxon 1945) and included the use of zero differences in the test (Pratt 1959). The use of these nonparametric tests allows for statistical analysis without the assumption of a specific distribution. Any significant differences between case types at G or F and any significant changes during the times leading up to both are highlighted in their respective figures at the 5% level ($p \leq 0.05$). The statistical tests were applied as one-sided tests when variables were hypothesized to be lower or higher in one set of cases than in the other.

3. Observations of bulk DSDs in hook echoes

After examination of a substantial number of cases using the thresholds outlined in section 2, 68 tornadic and 62 nontornadic supercells were selected for analysis throughout the contiguous United States (Fig. 3). Trends in the variables described in section 2, large and small drop gates, and relations to environmental characteristics preceding and during the time of G/F are also investigated.

a. Polarimetric radar attributes and bulk DSDs in tornadic and nontornadic hook echoes

We examine differences in Z_H, Z_{DR}, D_0, K_{DP}, and N_T for tornadic and nontornadic supercells at G and F to investigate

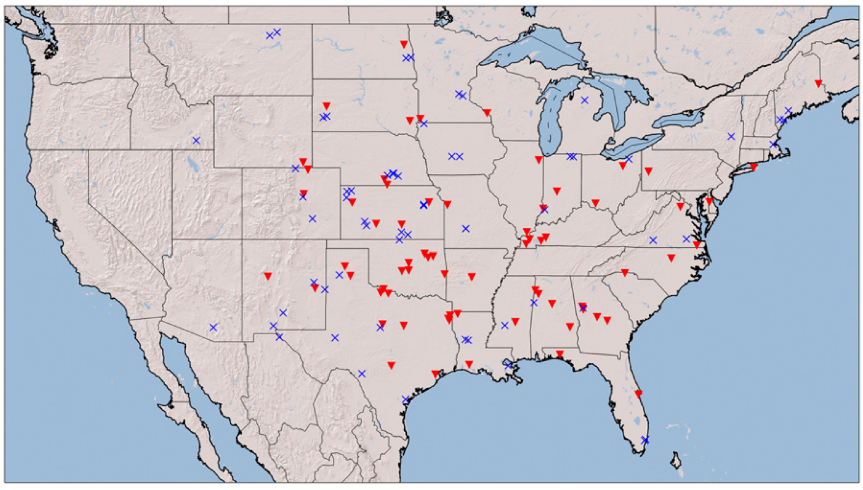

FIG. 3. The location of all tornadogenesis events (red inverted triangles) and all tornadogenesis failure events (blue X marks) analyzed for this study.

potential microphysical differences between case types as tornadoes develop or fail to develop. For this aspect of the study, we tested the following hypotheses:

1) Z_{DR} and D_0 are smaller at G than at F, while the other variables display no significant difference at G and F.
2) Tornadic hook echoes are characterized by a higher (lower) percentage of radar gates characterized by "small" ("large") drops than nontornadic hook echoes at G and F.
3) Tornadic hook echoes have a maximum in small drop radar gates in the front hook echo quadrants, while small drop gates are more evenly spread in nontornadic hook echo quadrants.
4) Cases with a significant percentage (>10%) of radar gates characterized by small drops have lower LCLs.

First, we compare Z_H–Z_{DR} plots of tornadic and nontornadic hook echoes at the time of G and F (Fig. 4a). Of note is the almost complete overlap between the two case types, contrary to the smaller Z_{DR} observed in tornadic cases in Kumjian and Ryzhkov (2008). The only significant differences occur at $Z_H \geq 55$ dBZ, but there is large uncertainty at high Z_H owing to a smaller sample of radar gates. The median Z_{DR} lines also are compared to the empirical relationship between Z_H and Z_{DR} from Cao et al. (2008; Fig. 4b). Both case types have very similar DSDs which are consistently higher than the Cao et al. (2008) Z_H–Z_{DR} relationship for values of $Z_H \leq \sim 47$ dBZ. Again, the only real differences between case types occur at high values of Z_H in which the number of gates sampled drops off considerably (not shown). Also, the median lines are much closer to the Cao et al. (2008) curve than that shown in Kumjian and Ryzhkov (2008).

Analysis of Z_H provides essentially no differences in distributions between tornadic and nontornadic hook echoes at G/F for any of the ranges analyzed (Fig. 5). There are no significant differences for Z_H between case types at G/F and therefore a null hypothesis that there is no difference between the two case types cannot be rejected. Similarly, Z_{DR} and D_0 exhibit few differences between tornadic and nontornadic cases (Fig. 6). For example, the smallest p values were 0.640 and 0.657 for Z_{DR} and D_0, respectively, in the interval $35 \leq Z_H < 40$ dBZ (Figs. 6b,f). Therefore, based on the results shown in Figs. 4 and 6, the hypothesis that tornadic cases have lower hook echo Z_{DR} is not supported in this study.

Also analyzed at G/F were K_{DP} and N_T (Fig. 7). As with Z_H, Z_{DR}, and D_0, K_{DP} shows no appreciable difference between case types at G/F (Figs. 7a–d). Using a two-sided test, the smallest p value for K_{DP} is 0.711 ($35 \leq Z_H < 40$ dBZ) and thus we cannot reject the null hypothesis that there is no difference in K_{DP} between the two case types. However, for all Z_H ranges, the distribution of nontornadic hook echoes have slightly higher medians of N_T than those in tornadic hook echoes at the same time (Figs. 7e–h). Though, as with previous results, none of these ranges show significant differences between case types (smallest p value of 0.246 for $40 \leq Z_H < 45$ dBZ).

To examine the higher and lower limits of the Z_{DR} distribution at G and F, "small" and "large" drop radar gates were defined as those with Z_{DR} values exceeding ±1.0 dB from the Cao et al. (2008) curve, respectively (e.g., Kumjian 2011). In total, the percentage of large drop gates is far higher than that for small drop gates in both sets of cases (Fig. 8). There is no indication that tornadic cases contain a higher percentage of small drop gates than nontornadic cases, counter to our hypothesis. Tornadic hook echoes contain more large drop gates than nontornadic hook echoes, but the results are not statistically significant (p value of 0.193).

To investigate spatial differences between tornadic and nontornadic hook echoes at G/F, the hook echoes were divided into quadrants. Table 1 shows which quadrants contain the largest number of small or large drop gates for each case. Percentages are used because not all hook echoes contain "small drop" or "large drop" gates; 60.29% (74.19%) of tornadic (nontornadic) cases have at least one gate defined as a small drop gate and 100% (93.55%) of tornadic (nontornadic) cases had at least one gate defined as a large drop gate at G/F.

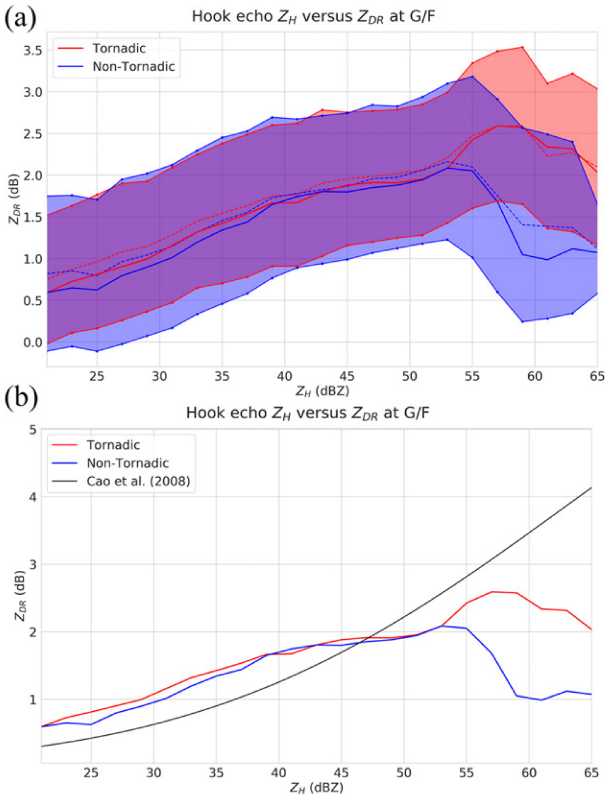

FIG. 4. (a) Comparison of Z_H and Z_{DR} for tornadic and nontornadic supercell hook echoes at G/F. The thick red (blue) lines denote the median Z_{DR} value for a given Z_H for tornadic (nontornadic) supercell hook echoes, and thin dashed red (blue) lines denote mean Z_{DR} for the same respective quantities. Thin solid lines denote ±1 standard deviation from their respective mean lines. The area shaded in purple shows where the tornadic and nontornadic Z_{DR} values overlap and the light red (light blue) shaded regions represent Z_{DR} values for only tornadic (nontornadic) hook echo values. (b) Comparison of Z_H, Z_{DR}, and the Cao et al. (2008) curve for tornadic and nontornadic supercell hook echoes at G/F.

Tornadic hook echoes have the largest percentage of cases with small drops in the LF quadrant, consistent with results from Kumjian (2011). Nontornadic hook echoes have the largest percentage of cases with small drops in the LB quadrant; tornadic cases, by comparison have far fewer small drop gates in the LB quadrant. But overall, both tornadic and nontornadic hook echoes have the most small drops in the LF and LB quadrants. The LF and RF quadrants show similar percentages of cases containing maximum amount of large drop gates; however, the LB and RB quadrants are structured differently. Tornadic storms have approximately twice the percentage of cases with large drop maximums in the LB quadrant. Nontornadic storms have approximately twice the percentage of cases with large drop maximums in the RB quadrant than in tornadic cases.

The analyses shown thus far were redone for tornadic cases separated out by EF-rating to determine if hypothesized signals are more apparent for strongly tornadic (19) rather than

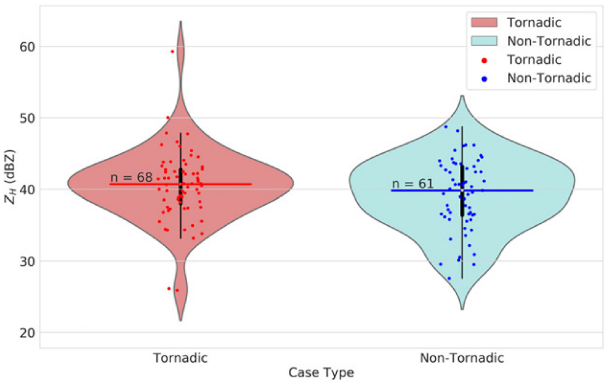

FIG. 5. Distributions of tornadic (red) and nontornadic (blue) hook echo median Z_H values at G/F for $Z_H \geq 20$ dBZ. The thick, black vertical lines denote the interquartile ranges. The thin, black lines extending below and above the interquartile ranges extend to the 5th and 95th percentiles, respectively. The horizontal red (blue) line denotes the median Z_H value for tornadic (nontornadic) cases. The number on each represents the number of cases that exceeded the thresholds specified in section 2.

weakly tornadic (49) cases. At G, for $Z_H \geq 20$ dBZ, hook echo median Z_H is approximately 3 dB lower in strongly tornadic storms than in weakly tornadic storms (Fig. 9a) and the difference is significant (p value of 0.0319). However, for all binned Z_H ranges, Z_{DR} is not statistically different between weakly and strongly tornadic storms (not shown) and the Z_{DR} distributions of weakly and strongly tornadic storms are similar overall (Fig. 9b). The most apparent difference occurs at $40 \leq Z_H < 45$ dBZ in which strongly tornadic hook echoes show ~0.5 dB higher median Z_{DR} than the weakly tornadic hook echoes (Fig. 9c); however, the signal may be an artifact of the increasing amount of data parsing and small sample of cases. D_0 exhibits similar results to Z_{DR}, where for $40 \leq Z_H < 45$ dBZ, strongly tornadic storms have drops that are about 0.5 mm larger than weakly tornadic storms (not shown). However, none of the binned Z_H ranges for strongly and weakly tornadic D_0 are significantly different from one another (e.g., Fig. 9d). The K_{DP} shows more obvious discrepancies between weakly and strongly tornadic hook echoes (Figs. 9e,f). For binned Z_H range $35 \leq Z_H < 40$ dBZ (Fig. 9e), weakly and strongly tornadic hook echo K_{DP} are statistically different from one another (p value of 0.0346). All four binned Z_H ranges show strongly tornadic hook echoes exhibiting lower median K_{DP} than weakly tornadic hook echoes. The distributions of N_T at G for strongly and weakly tornadic storms are similar, with the exception of $40 \leq Z_H < 45$ dBZ (Fig. 9f), where median N_T for strongly tornadic storms is ~330 m^{-3} lower than weakly tornadic storms. However, the distributions are not significantly different from each other.

At G, the percentage of hook echo small and large drop gates is similar between weakly and strongly tornadic hook echoes (Fig. 10). Strongly tornadic hook echoes have less variability in their small drop distribution, show slightly more variability in their large drop distribution, and have a higher median value than weakly tornadic hook echoes. Overall, none

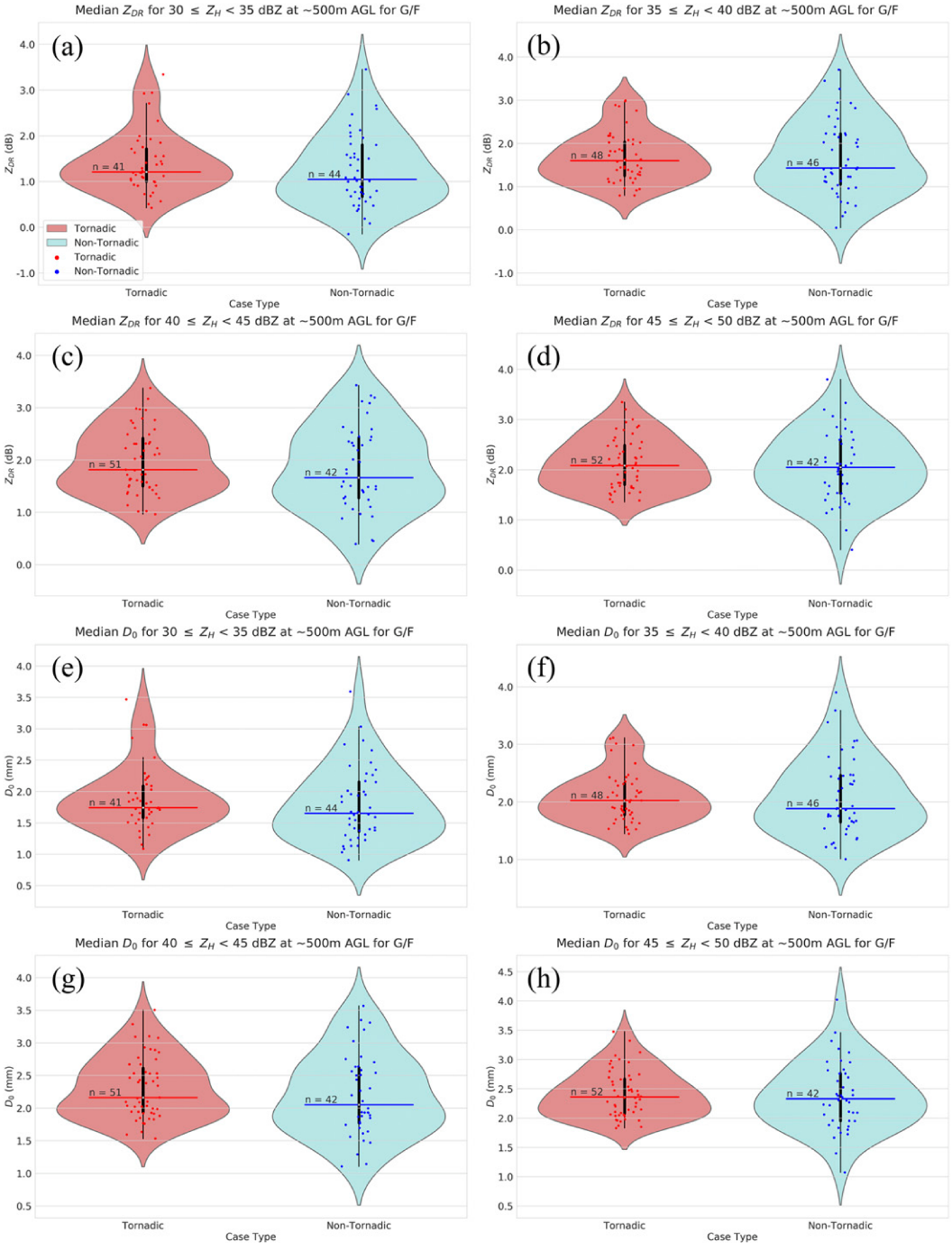

FIG. 6. As in Fig. 5, but for hook echo median (a)–(d) Z_{DR} and (e)–(h) D_0 values.

of the hypothesized relationships become more apparent when separating out tornadic cases by intensity.

Cases also were broken down by EF scale to determine if the spatial distribution of large and small drops may play a role in the intensity of an ensuing tornado. Table 2 shows the same tornadic percentages as presented in Table 1, but broken down into the weakly and strongly tornadic categories. Both weakly tornadic and strongly tornadic storms have the highest percent of cases with the maximum in small drop gates occurring in the LF quadrant. In nontornadic cases, there is a much larger percentage of cases with the most small drop gates in the LB quadrant, compared to strongly tornadic storms, which have small drop gates concentrated in the RB quadrant. The location where the most large drop gates occurs for strongly tornadic storms is split between the LF and LB quadrants. Of note is the LF quadrant, where 31.58% of strongly tornadic storms,

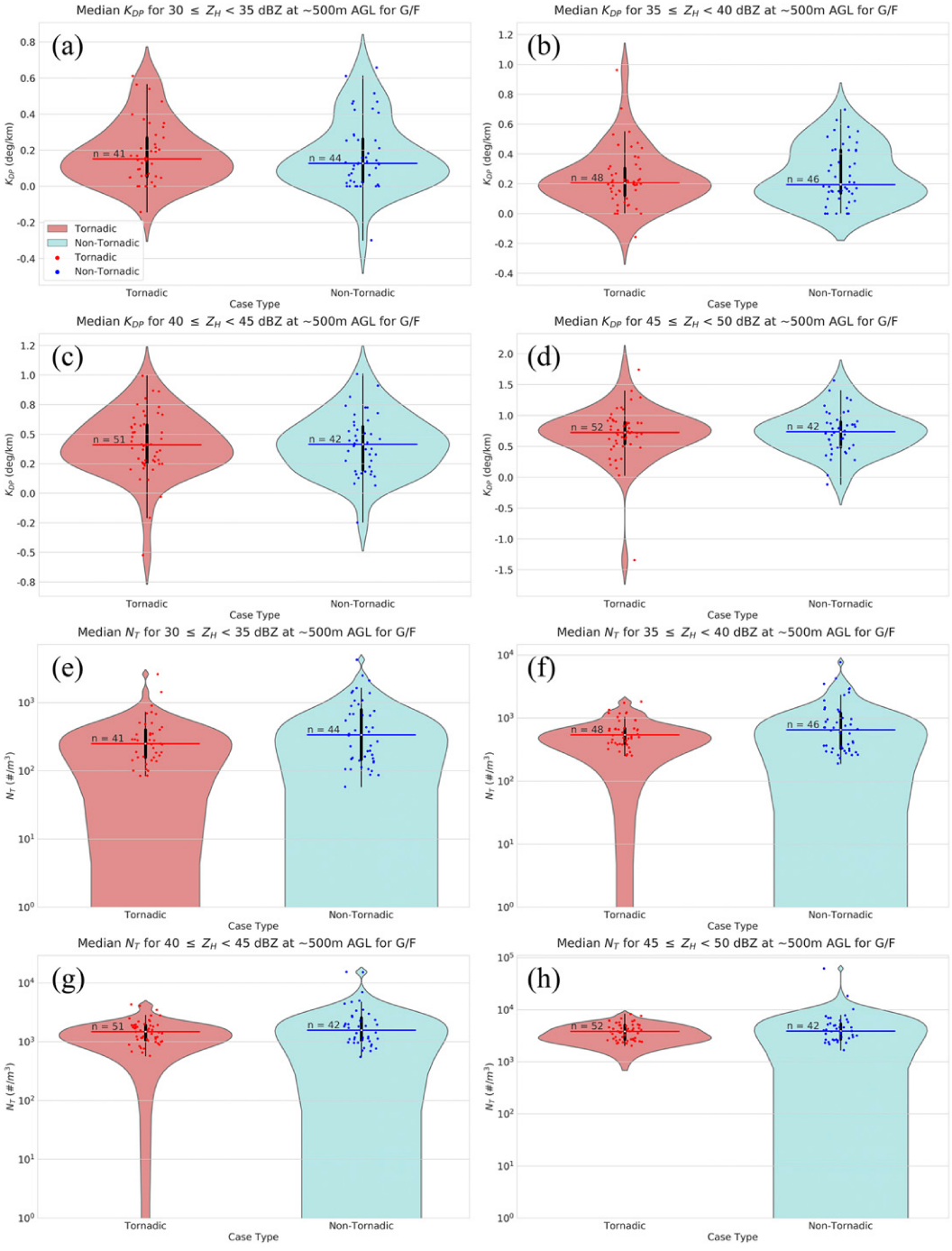

FIG. 7. As in Fig. 5, but for hook echo median (a)–(d) K_{DP} and (e)–(h) N_T values.

10.20% of weakly tornadic, and 11.29% of nontornadic storms have the most large drops.

As expected, tornadic hook echoes tend toward lower LCLs for the same value of median Z_{DR} at G as nontornadic hook echoes at F, but there is a substantial amount of spread (Fig. 11a). However, the scatterplots show no obvious linear relationship between the various estimates of drop size and LCL height for either tornadic or nontornadic cases. For example, even the cases with large percentages (>10%) of small drop gates have highly variable LCLs (Fig. 11b). Similarly, cases with both small (<10%) and large (>50%) percentages of large drop gates occur in environments that run a large range of LCLs (Fig. 11c). Overall, there is no obvious direct link between Z_{DR}, small and large drop sizes, and LCLs in this study. Other NSE variables analyzed include 0–1-km SRH and shear vector magnitude. As with LCLs, there

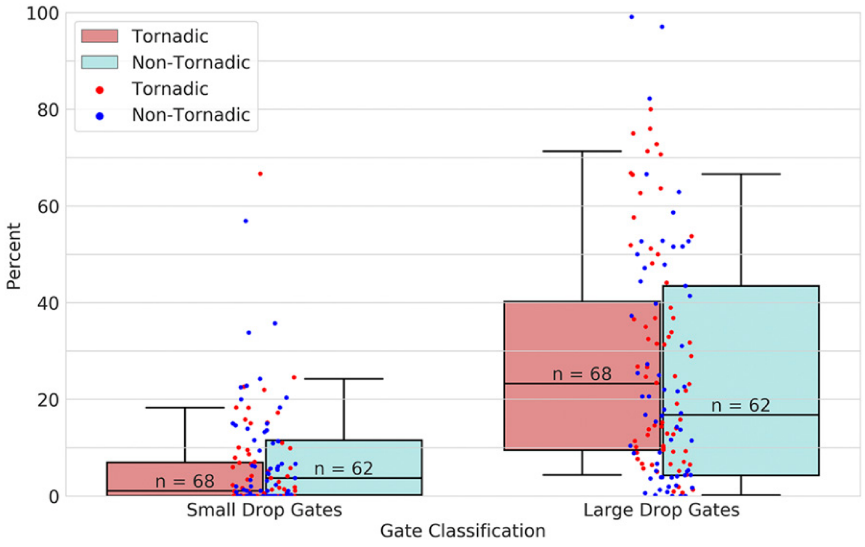

FIG. 8. Boxplots showing the distributions of the percentage of hook echo gates characterized by (left) small drops and (right) large drops for tornadic (red) and nontornadic (blue) hook echoes at G/F. The number shows how many cases were considered for each.

is substantial variability in 0–1-km SRH and 0–1-km shear vector magnitude for small and large percentages of small drop gates and large drop gates (not shown). These results suggest that NSE characteristics probably do not play a substantial role in short time scale changes in hook echo DSDs.

b. *Trends in hook echo bulk DSDs*

Analysis of polarimetric, derived, and environmental variables at G/F provides some idea of differences between tornadic and nontornadic supercell hook echoes. However, analysis only at G/F gives an incomplete picture of the entire process preceding tornadogenesis and tornadogenesis failure. As such, times prior to tornadogenesis and tornadogenesis failure were analyzed to investigate any differences between these two case types during the minutes leading up to these events. In this section, we test the following hypotheses:

1) Hook echo Z_{DR} and D_0 decrease leading up to tornadogenesis but not leading up to tornadogenesis failure, and there are no observable differences among case sets for other variables.
2) The percentage of small (large) drop gates increase (decrease) prior to tornadogenesis, but there is no discernable trend in the percentage of small or large drop gates leading up to tornadogenesis failure.
3) Cases that exhibit decreases in Z_{DR} and D_0 prior to tornadogenesis (failure) occur in environments with lower LCLs.

More separation occurs between the DSDs of tornadic and nontornadic supercells in the time before tornadogenesis and tornadogenesis failure than at G/F (e.g., Fig. 12), but there is still considerable overlap between the two sets of storms, and the separation is counter to that hypothesized in previous studies. The Z_{DR} separation is maximized (~0.5 dB difference) at $45 < Z_H \leq 55$ dBZ at G-3/F-3 (Fig. 12b). At subsequent times (not shown), the Z_{DR} separation is typically less, consistent with that shown in Fig. 4. In addition, because of the decrease in the number of gates with increasingly higher values of Z_H in this range, any differences between case types at $Z_H > 55$ dBZ are too uncertain to draw conclusions from.

During the time leading up to tornadogenesis and tornadogenesis failure, there is a noticeable increase in median hook echo Z_H in tornadic cases from G-4 to G and a decrease for nontornadic cases from F-4 to F-3 followed by a subtle increase from F-3 to F. (Fig. 13a). None of the times prior to G/F are

TABLE 1. A table of the percentage of cases where the most small drops occurred (top) and where the most large drops occurred (bottom) in a given quadrant for tornadic and nontornadic hook echoes at G/F.

LB quadrant	Tornadic	Nontornadic	LF quadrant	Tornadic	Nontornadic
Small %	16.18	29.03	Small %	27.94	25.81
RB quadrant	Tornadic	Nontornadic	RF quadrant	Tornadic	Nontornadic
Small %	8.82	6.45	Small %	7.35	12.90
LB quadrant	Tornadic	Nontornadic	LF quadrant	Tornadic	Nontornadic
Large %	30.88	16.13	Large %	16.18	11.29
RB quadrant	Tornadic	Nontornadic	RF quadrant	Tornadic	Nontornadic
Large %	20.59	38.71	Large %	32.35	27.42

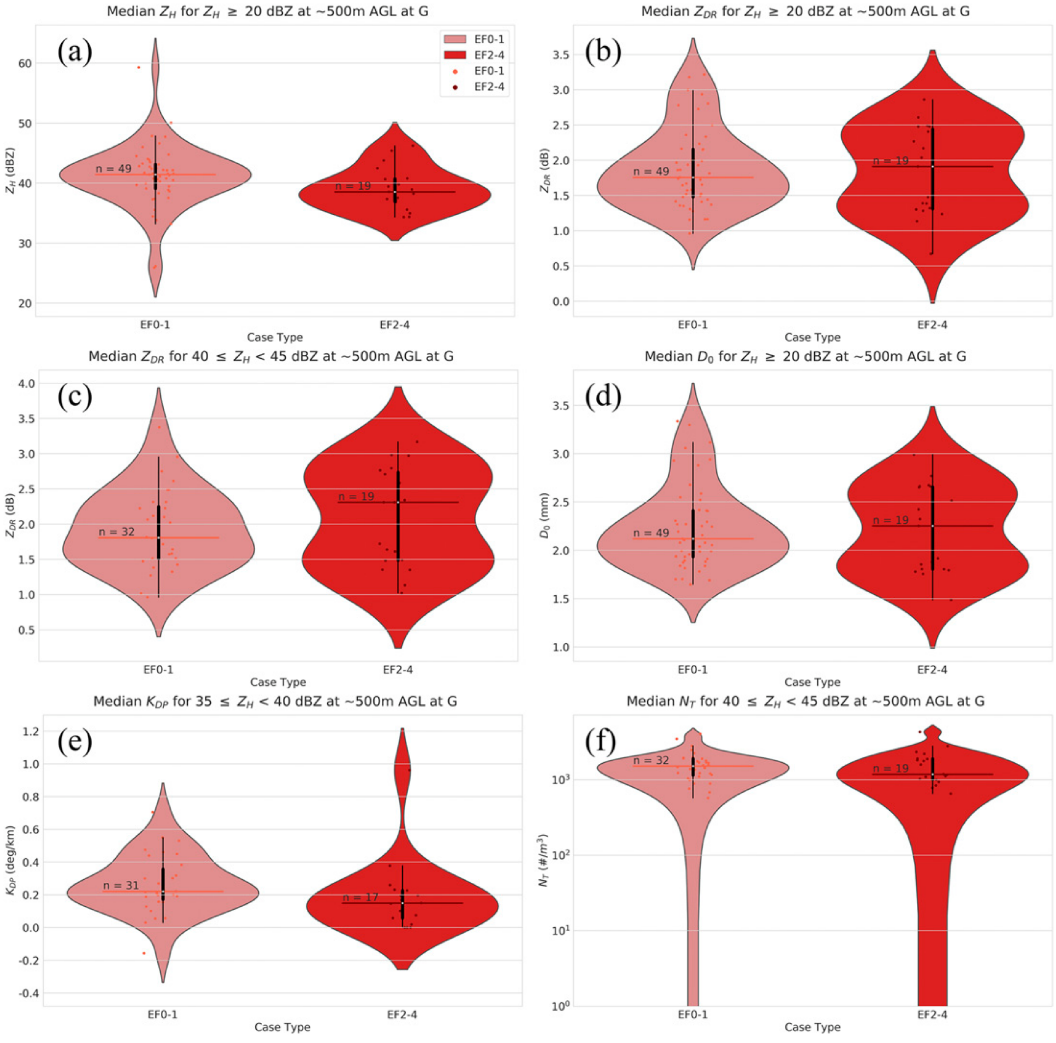

FIG. 9. As in Fig. 5, but for hook echo median (a) Z_H for $Z_H \geq 20$ dBZ, Z_{DR} for (b) $Z_H \geq 20$ dBZ and (c) $40 \leq Z_H < 45$ dBZ, (d) D_0 for $Z_H \geq 20$ dBZ, (e) K_{DP} for $35 \leq Z_H < 40$ dBZ, and (f) N_T for $40 \leq Z_H < 45$ dBZ for weakly tornadic (pink) and strongly tornadic (red). The p values from the Mann–Whitney U tests for the two-tailed test are $p = 0.0319$ in (a) and $p = 0.0346$ in (e).

statistically significantly different from G/F using a two-sided test at 95% confidence. Based on the results shown in Figs. 5 and 13a, hook echo Z_H alone does not possess discriminatory power between tornadic and nontornadic supercells.

During the same time period, *Z_{DR} tends to decrease overall for both case types* (Fig. 13b). However, the main discrepancy between case types occurs during the 5-min period between G-4/F-4 and G-3/F-3. For $30 \leq Z_H < 40$ dBZ (Fig. 13c), Z_{DR} exhibits a decrease in Z_{DR} of ~0.3 dB for tornadic cases and is relatively constant for $40 \leq Z_H < 50$ dBZ (Fig. 13d). On the contrary, nontornadic cases show increases in Z_{DR} for the same 5-min period for $30 \leq Z_H < 40$ dBZ and $40 \leq Z_H < 50$. The F-4 scan for $Z_H \geq 20$ dBZ is the only scan that is statistically different from F for Z_{DR} (Fig. 13b).

The D_0 also decreases for both tornadic and nontornadic hook echoes leading up to tornadogenesis and tornadogenesis failure (Fig. 13e). However, D_0 exhibits a similar discrepancy between case types as Z_{DR} for $30 \leq Z_H < 35$ dBZ, $40 \leq Z_H < 45$ dBZ, and $45 \leq Z_H < 50$ dBZ (not shown) during the G-4/F-4 to G-3/F-3 period. During this 5-min period, D_0 decreases (increases) in tornadic (nontornadic) hook echoes. This difference in behavior is most pronounced for $30 \leq Z_H < 35$ dBZ and becomes less apparent for higher ranges of Z_H. The D_0 also decreases slightly more during the period in nontornadic hook echoes than in tornadic hook echoes.

For all binned Z_H ranges, nontornadic hook echo median Z_{DR} decreases more than their tornadic counterparts during the time leading to tornadogenesis and tornadogenesis failure, but by small amounts (Fig. 13f). The total changes in Z_{DR} for $Z_H \geq 20$ dBZ leading up to G and F do lean toward decreasing trends, but are short of significance (p values of 0.129 and 0.092 respectively), and the two case type distributions are not significantly different from one another. Likewise, D_0 generally decreases more during the time leading up to F than G

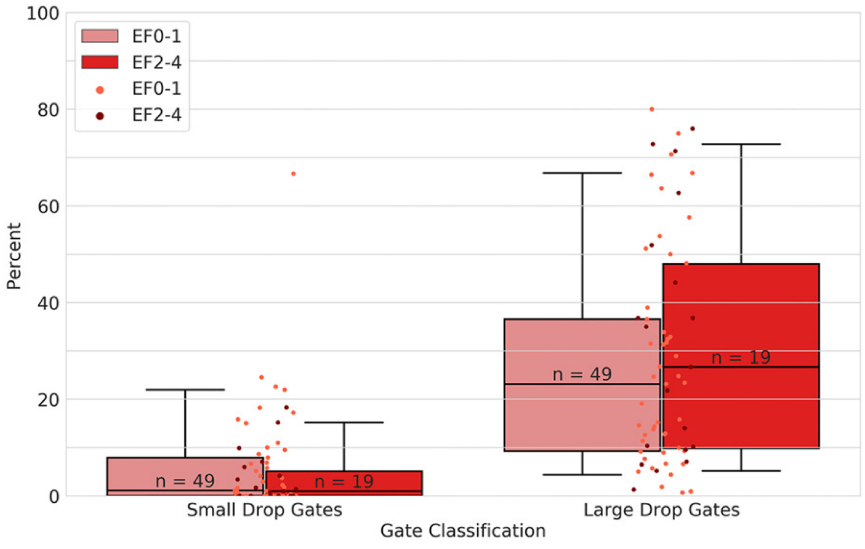

FIG. 10. As in Fig. 8, but for weakly tornadic (pink) and strongly tornadic (red).

(Fig. 13g). Neither the total tornadic or nontornadic D_0 changes for $Z_H \geq 20$ dBZ are statistically significant and the two distributions of D_0 changes are not statistically significantly different from one another.

The K_{DP} values during the time preceding G and F are variable for nontornadic hook echoes and show a slight increase for tornadic hook echoes (Fig. 14a). Median K_{DP} values tend to be larger for all binned Z_H ranges in nontornadic hook echoes. Both tornadic and nontornadic hook echoes show general increases in N_T during the period of interest (Fig. 14b). As with Z_{DR} and D_0, N_T shows a difference in behavior for $30 \leq Z_H < 35$ dBZ, $40 \leq Z_H < 45$ dBZ, and $45 \leq Z_H < 50$ dBZ (not shown) from G-4/F-4 to G-3/F-3. During this 5-min period, N_T increases for tornadic hook echoes and decreases for nontornadic hook echoes. The most notable difference between changes in N_T during this time occurs for $30 \leq Z_H < 35$ dBZ where median tornadic N_T increases by approximately 100 m^{-3} and median nontornadic N_T remains relatively steady. None of the scans prior to G/F are statistically different from G/F.

The total change histograms of K_{DP} (Fig. 14c) and N_T (Fig. 14d) show that the distributions are largely similar and overlap considerably. There is a slight skew toward increasing (decreasing) K_{DP} values for tornadic (nontornadic) hook echoes. However, the two change distributions are centered near zero and are not statistically different from zero or from one another. Both tornadic and nontornadic hook echoes lean toward increasing N_T, but neither increase is statistically significant and the total change distributions of tornadic and nontornadic N_T are not significantly different from one another.

During the time leading up to G and F, nontornadic hook echoes tend to have more small drop gates than tornadic hook echoes (Fig. 15a). Tornadic small drop percentages are lower and show little change whereas nontornadic small drop percentages tend to increase in variability during the time preceding tornadogenesis failure. The G-3 scan time was the only one that was statistically different from G (p value of 0.0237). Conversely, tornadic hook echoes had a higher percentage of large drop gates than nontornadic hook echoes (Fig. 15b). One of the clearest signals seen in this study is that both case types exhibit decreases in the percentage of large drop gates from G-4/F-4 to G-2/F-2, but these decreases level off after G-2/F-2. The F-4 and F-3 scans were both significantly different from F (p values of 0.0332 and 0.0459, respectively). Most of the total changes in small drop percentage are small (Fig. 15c). The peak in the change of tornadic small drop gate percentage is in the

TABLE 2. A table of the percentage of cases where the most small drops occurred and where the most large drops occurred (bottom) in the left back (LB), left front (LF), right back (RB), and right front (RF) quadrants for weakly tornadic (EF0–1), strongly tornadic (EF2–4), and nontornadic hook echoes at G/F.

LB quadrant	EF0–1	EF2–4	Nontornadic	LF quadrant	EF0–1	EF2–4	Nontornadic
Small %	18.37	10.53	29.03	Small %	30.61	21.05	25.81
RB quadrant	EF0–1	EF2–4	Nontornadic	RF quadrant	EF0–1	EF2–4	Nontornadic
Small %	6.12	15.79	6.45	Small %	6.12	10.53	12.90
LB quadrant	EF0–1	EF2–4	Nontornadic	LF quadrant	EF0–1	EF2–4	Nontornadic
Large %	30.61	31.58	16.13	Large %	10.20	31.58	11.29
RB quadrant	EF0–1	EF2–4	Nontornadic	RF quadrant	EF0–1	EF2–4	Nontornadic
Large %	20.41	21.05	38.71	Large %	38.78	15.79	27.42

FIG. 11. Scatterplots showing tornadic (red) and nontornadic (blue) hook echo (a) median Z_{DR} at G/F, (b) small drop gate percentage, and (c) large drop gate percentage vs LCL height. The numbers in the legend show how many cases are considered for each case type and are the same for (a)–(c).

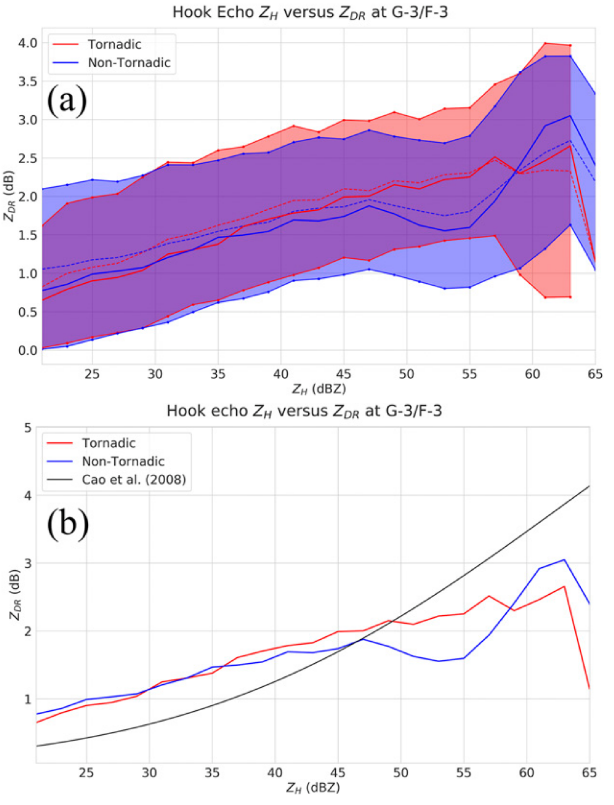

FIG. 12. As in Fig. 4, but for G-3/F-3.

range from 0% to −5%, while the total changes are almost evenly split between increasing and decreasing percentages for nontornadic cases. A majority of both tornadic and nontornadic cases exhibit an overall decrease in the percentage of large drop gates (Fig. 15d), but neither of the large drop percentage change distributions are significantly different from zero and are not significantly different from one another.

Regardless of whether Z_{DR} increases or decreases during the time preceding tornadogenesis and tornadogenesis failure, tornadic storms tend to occur in environments with overall lower LCLs (Fig. 16). There is little difference in LCLs between cases that undergo Z_{DR} increases and decreases regardless of case type. However, there is a significant difference between LCLs for tornadic and nontornadic cases that exhibit decreases in Z_{DR} prior to tornadogenesis and tornadogenesis failure (p value of 0.0130). Both 0–1-km SRH and 0–1-km shear vector magnitudes are higher in tornadic storms than in nontornadic storms regardless of whether Z_{DR} increased or decreased (not shown). These results suggest, as shown previously (Fig. 11), that NSE seems to play little role in shorter time scale differences in DSDs.

To investigate the sensitivity of the results to the rotational intensity of nontornadic supercells, the two aforementioned subsets of nontornadic supercells were compared to tornadic supercell cases, as in Figs. 13 and 14. The subset using the 25th percentile (one standard deviation below the mean) azimuthal shear threshold provided 32 (44) nontornadic cases for comparison. Thresholding these data in this way allowed for investigation of only strongly rotating nontornadic supercells. The results from these subsets were essentially identical to the comparison of the full nontornadic dataset to the tornadic dataset; therefore, we believe the full set of nontornadic results are not biased by weakly rotating nontornadic supercells (not shown).

4. Summary and discussion

Overall, an examination of 130 supercell hook echoes did not provide evidence to support many of the hypotheses

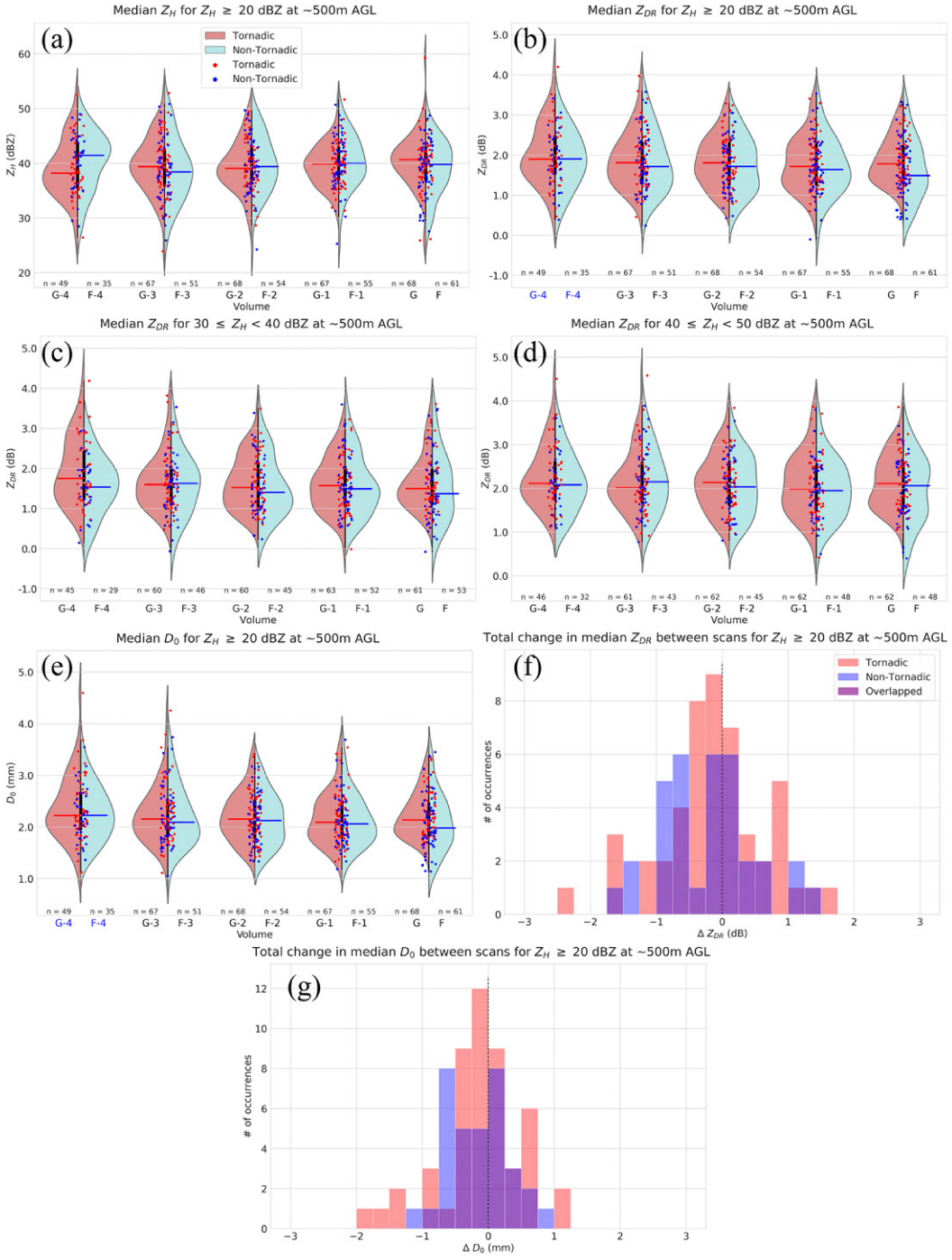

FIG. 13. Time series for tornadic (red) and nontornadic (blue) hook echoes for (a) median Z_H for $Z_H \geq 20$ dBZ, (b) Z_{DR} for $Z_H \geq 20$ dBZ, (c) Z_{DR} for $30 \leq Z_H < 40$ dBZ, (d) Z_{DR} for $40 \leq Z_H < 50$ dBZ, and (e) D_0 for $Z_H \geq 20$ dBZ. Abscissa labels colored blue indicate statistically significant differences from that scan to F for nontornadic storms. Tornadic (red) and nontornadic (blue) total change histograms for (f) median Z_{DR} for $Z_H \geq 20$ dBZ and (g) D_0 for $Z_H \geq 20$ dBZ. Purple denotes overlap between the two total change distributions. Vertical, dashed, black lines denote the zero-change line of the histograms in (f) and (g). The p values from the one-tailed Wilcoxon tests with the null hypothesis that nontornadic Z_{DR} and D_0 do not decrease leading up to F for the statistically significant nontornadic changes highlighted in blue are 0.0109 in (b) and 0.0173 in (e).

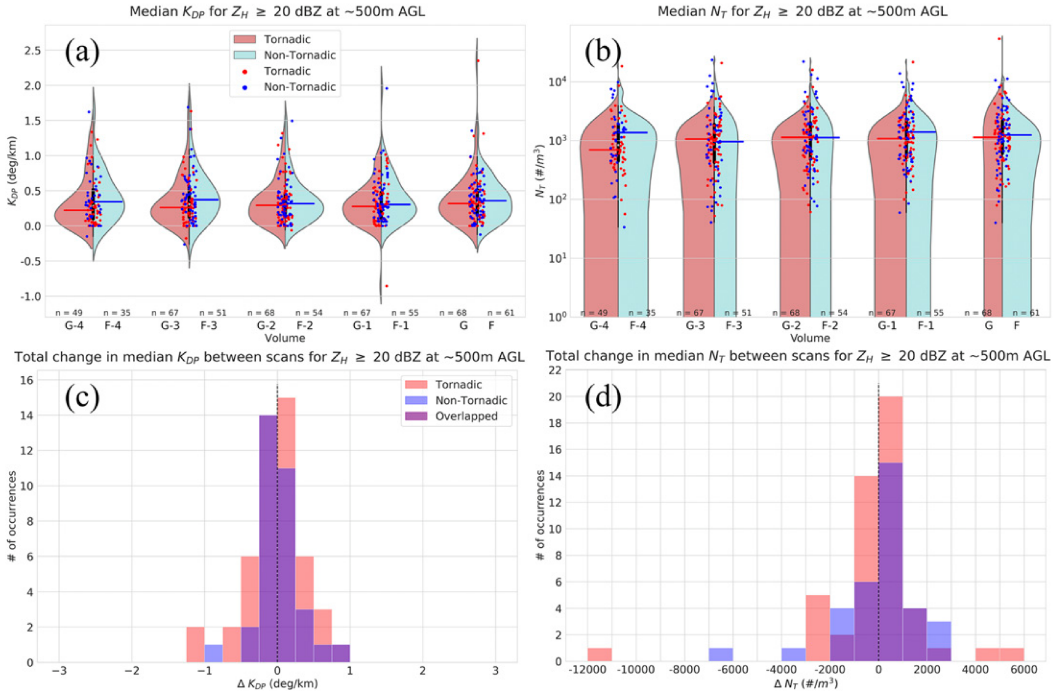

FIG. 14. As in Figs. 13b–e, but for (a),(c) K_{DP} and (b),(d) N_T.

developed based on past studies and failed to identify obvious differences between tornadic and nontornadic cases at the time of tornadogenesis or tornadogenesis failure. There was essentially no separation between median Z_{DR} and drop sizes of tornadic and nontornadic supercells (Fig. 4), and tornadic hook echoes did not contain more small drops at G than nontornadic hook echoes at F (Fig. 8). These results are contrary to our hypotheses and results found in Kumjian and Ryzhkov (2008) and French et al. (2015). Separating tornado cases by intensity did not provide markedly different conclusions (Figs. 9–10). However, strongly tornadic hook echoes showed significantly lower Z_H and K_{DP} at G than weakly tornadic hook echoes at the same time (Figs. 9a,e). These discrepancies in strongly and weakly tornadic hook echoes may indicate that there were less evaporative cooling effects in strongly tornadic hook echoes than in weakly tornadic storms. And dividing cases into nontornadic, weakly tornadic, and strongly tornadic storms may provide better insight into the ongoing processes which dictate tornadogenesis potential and tornado intensity potential. In addition, the environmental analyses did not provide evidence of a relationship between LCLs and drop size as shown in French et al. (2015); there were also no relationships between drop sizes and either 0–1-km SRH or 0–1-km shear vector magnitude. However, at G/F, both sets of cases tended to have small drop gates in the LF quadrant (Table 1), which is consistent with the results described in Kumjian (2011), and when tornadic storms were broken down by surveyed tornado intensity (Table 2), strongly tornadic hook echo drop sizes matched closest to the conceptual supercell model results presented in Kumjian (2011).

The other main aspect of this study was determining trends in hook echo polarimetric variables and approximated bulk DSDs. There, as well, results generally did not support hypotheses. The Z_{DR} and D_0 generally decreased leading up to tornadogenesis, consistent with French et al. (2015); however, both quantities also decrease leading up to tornadogenesis failure. Changes in small drop percentage for both sets of cases were small, and though large drop percentages did decrease leading up to tornadogenesis as hypothesized, the same trend again was seen leading up to tornadogenesis failure. Finally, cases that exhibited decreases in Z_{DR} leading up to tornadogenesis (failure) did not generally occur in environments with lower LCLs compared to those that exhibited no change in Z_{DR} or Z_{DR} increases.

There were several other observations made outside of our hypotheses, some of which warrant further discussion. Nontornadic storms exhibited a high percentage of cases where the most small drop gates occurred in the LB quadrant. Large drop gates were common in the LB (RB) for tornadic (nontornadic) cases. Both weakly and strongly tornadic storms favored large drop gates in the LB quadrant, while nontornadic storms favored the RB quadrant. The LF quadrant showed a substantially larger percent of strongly tornadic cases which had the most large drops here than weakly and nontornadic storms. One speculative possibility is that, if we assume air generally travels cyclonically from LB to RB to RF to LF quadrants before entering the low-level updraft, the shorter (longer) distance between the large (small) drops and attendant less (more) buoyant air to the nontornadic cases compared to the tornadic cases may influence vortex evolution at the margins. Nonetheless, observing the entire hook echo as a

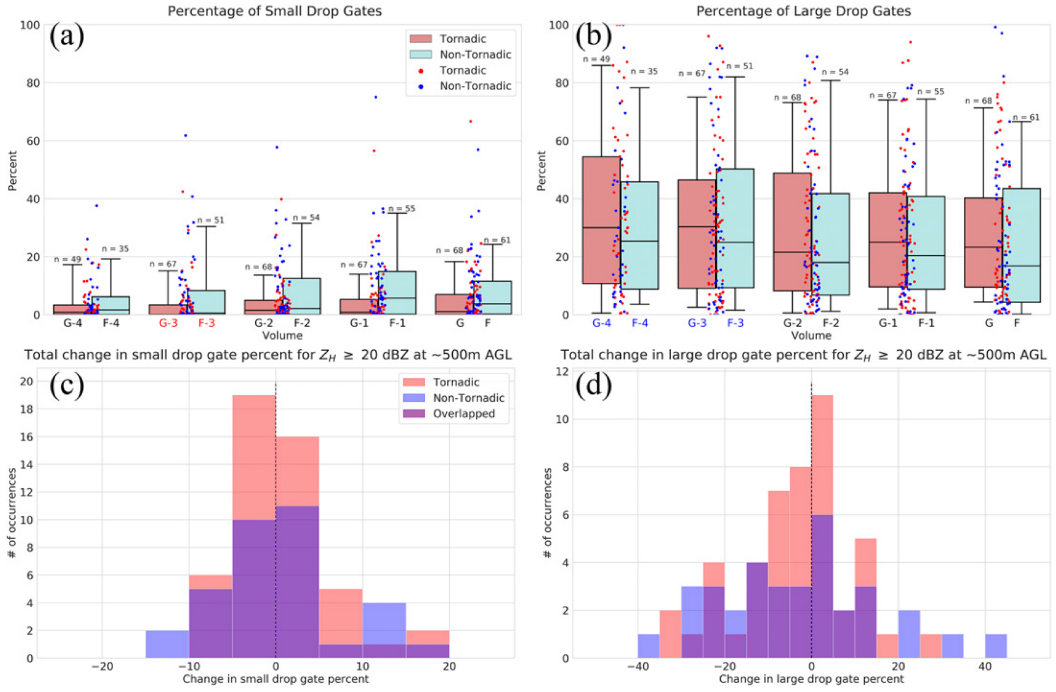

FIG. 15. As in Fig. 14, but for (a),(c) small drop gate percentage and (b),(d) large drop gate percentage. Abscissa labels in red (blue) denote statistically significant differences from G (F) for tornadic (nontornadic) cases. The p values for the two-sided Wilcoxon tests for significant differences from G for small drop percentage is from G-3 to G, $p = 0.0237$ in (a), and from F for large drop percentage from F-4 to F, $p = 0.0332$, and F-3 to F, $p = 0.0459$ in (b).

whole may obscure smaller-scale changes within the hook echo that may be important to tornadogenesis or tornadogenesis failure.

Tornadic and nontornadic hook echo DSDs exhibit similar trends leading up to tornadogenesis (failure). The Z_{DR} and D_0 both generally decrease, K_{DP} exhibits little change, and N_T generally increases during these times (Figs. 13–14). However, tornadic cases show a general increase in Z_H and nontornadic cases show a general decrease. One interpretation of these results is that Z_{DR}, D_0, and N_T behave similarly for tornadic and nontornadic cases, but not for the same reason. A decrease in D_0 would tend to drive Z_H down assuming N_T remained constant, and an increase in N_T would tend to drive Z_H up assuming D_0 remained constant. However, in this study, D_0 generally decreased and N_T generally increased. Since there is a discrepancy in Z_H despite similar behaviors in D_0 and N_T, it suggests that the increase in N_T might explain the increase in Z_H for tornadic hook echoes, whereas the decrease in D_0 might be the reason for the decrease in Z_H for nontornadic hook echoes. Whether either of these changes are driven primarily by evaporation rate remains unclear. Kumjian and Ryzhkov (2010) found at S-band that, in areas of evaporation, Z_H and K_{DP} both substantially decreases while Z_{DR} slightly increases. Since an influx of drops appears to occur in both case types, any signal from evaporation occurring within these hook echoes may be obscured. It is possible, however, that the decrease in Z_H with little change in K_{DP} and a decrease in Z_{DR} could signal an influx of smaller drops in addition to ongoing evaporation within nontornadic hook echoes. *Therefore, one possibility is that the trend of decreases in Z_{DR} and D_0 and increase in N_T regardless of case type may indicate that an associated influx of less negatively buoyant RFD region air is associated with an increase in low-level rotation, but not necessarily tornado production.* Given the complexity of the latter, we believe it is reasonable that at G/F, the thermodynamic characteristics of air being ingested by the storm may be favorable, but the presence or absence of other needed processes (e.g., generation of near-surface horizontal vorticity, low-level dynamic lifting, etc.) separate out the tornadic from the nontornadic cases.

When observing the time series of hook echo small and large drop percentages, it is shown that nontornadic hook echoes tend to have more (fewer) small (large) drop gates than tornadic hook echoes for all times analyzed preceding tornadogenesis and tornadogenesis failure (Fig. 15). This is contrary to previous literature, where it was suggested that tornadic hook echoes may have smaller drops than nontornadic hook echoes. Both case types showed a general decrease in the amount of large drops present during the time preceding G/F. While this supports the hypothesis that large drops decrease prior to tornadogenesis presented in French et al. (2015), the fact that nontornadic supercells exhibit the same behavior again suggests that this may be associated with an increase in low-level rotation (and potentially an increase in size sorting) rather than a sufficient condition for tornadogenesis.

Taken as a whole, these results do not generally support the use of bulk estimated hook echo DSDs and hook echo polarimetric variables in nowcasting supercell tornado formation.

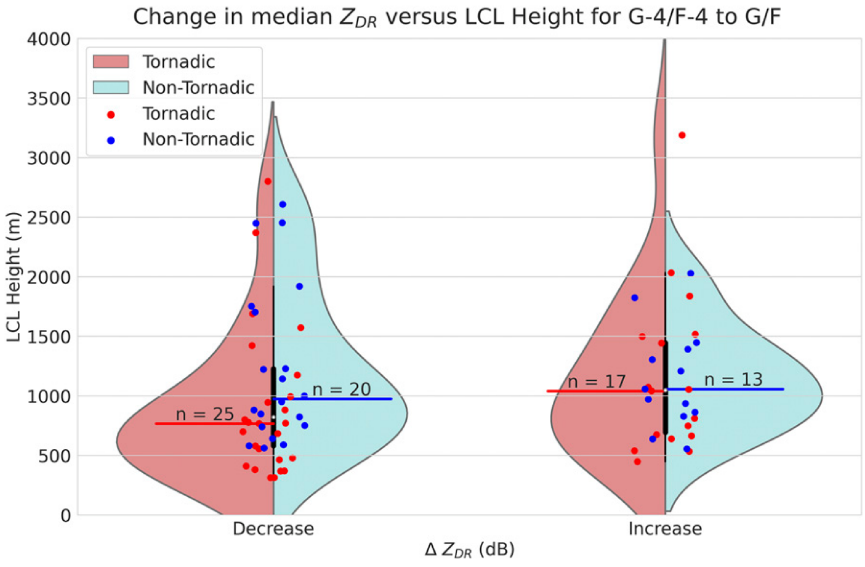

FIG. 16. Violin plots showing the median LCL height based on whether the total change in median Z_{DR} from G-4/F-4 to G/F increased or decreased for tornadic (red) and nontornadic (blue) storms. The p values for one-tailed Mann–Whitney U tests with the null hypothesis nontornadic cases have lower LCLs than tornadic cases are 0.0130 for cases where Z_{DR} decreased.

There are some significant differences at some time steps for some variables, but there are no systematic hypothesis-supported differences between tornadic and nontornadic cases. Why? Previous studies did rely on small samples of cases. Beyond that, we believe there is evidence to support that some of the DSD behaviors are associated with the hypothesized thermodynamic influences. However, as discussed previously, the processes needed for tornadogenesis extend far beyond adequately buoyant air to the point that any DSD signal may be overwhelmed. Indeed, an emerging theme of recent work emphasizes the importance of the low-level wind field, shallow layer SRH, and the attendant low-level dynamic lifting rather than outflow buoyancy for supercell tornadogenesis (e.g., Coffer and Parker 2017, 2018; Coffer et al. 2017).

Further analysis of how drop sizes change in each hook echo quadrant during the time leading up to tornadogenesis or tornadogenesis failure is recommended, as it may be useful in discriminating between nontornadic, weakly tornadic, and strongly tornadic supercells in real-time, while the storms are developing. Analysis of Z_H, Z_{DR}, D_0, K_{DP}, and N_T for each individual quadrant may also provide insight into the physical processes ongoing within smaller regions of the hook echo that result in tornadogenesis or tornadogenesis failure. Ideally, the analysis of large sets of tornadic and nontornadic storms sampled with high-resolution, polarimetric mobile radar would be the logical next step to this study, but such a dataset does not yet exist. As such, high-resolution modeling, as done in Kumjian et al. (2015) will be needed to further clarify the differences in drop sizes between strongly tornadic, weakly tornadic, and nontornadic hook echoes and show where these drops originate.

Acknowledgments. We thank the three anonymous reviewers whose comments substantially improved the content and clarity of this manuscript. We also thank Pavlos Kollias and Brian Colle for suggestions and comments provided during the first author's M.S. thesis work at Stony Brook University. This study was supported by NSF Grant AGS-1748177 (French) and AGS-1748191 (Kingfield).

Data availability statement. The WSR-88D, RAP, and EF-scale rating data used in this study are publicly available through the National Centers for Environmental Information website (ncdc.noaa.gov). The generated subsets of edited tornadic and non-tornadic data comprise several hundred cases, including discarded cases, and the resulting files are too large to be maintained externally indefinitely. They are viewable in WDSS-II and can be accessed by contacting the corresponding author.

REFERENCES

Beck, J., and C. Weiss, 2013: An assessment of low-level baroclinity and vorticity within a simulated supercell. *Mon. Wea. Rev.*, **141**, 649–669, https://doi.org/10.1175/MWR-D-11-00115.1.

Benjamin, S. G., and Coauthors, 2016: A North American hourly assimilation and model forecast cycle: The Rapid Refresh. *Mon. Wea. Rev.*, **144**, 1669–1694, https://doi.org/10.1175/MWR-D-15-0242.1.

Brandes, E. A., 1978: Mesocyclone evolution and tornadogenesis: Some observations. *Mon. Wea. Rev.*, **106**, 995–1011, https://doi.org/10.1175/1520-0493(1978)106<0995:MEATSO>2.0.CO;2.

Brooks, H. E., C. A. Doswell III, and J. Cooper, 1994: On the environment of tornadic and nontornadic mesocyclones. *Wea. Forecasting*, **9**, 606–618, https://doi.org/10.1175/1520-0434(1994)009<0606:OTEOTA>2.0.CO;2.

Cao, Q., G. Zhang, E. Brandes, T. Schuur, A. Ryzhkov, and K. Ikeda, 2008: Analysis of video disdrometer and polarimetric radar data

to characterize rain microphysics in Oklahoma. *J. Appl. Meteor. Climatol.*, **47**, 2238–2255, https://doi.org/10.1175/2008JAMC1732.1.

Chrisman, J. N., 2013: Dynamic scanning. *NEXRAD Now*, No. 22, 12 pp., NOAA, https://www.roc.noaa.gov/WSR88D/PublicDocs/NNOW/NNow22c.pdf.

——, 2014: Multiple Elevation Scan Option for SAILS (MESO-SAILS)—The Next Step in Dynamic Scanning for the WSR-88D. WSR-88D Radar Operations Center, 27 pp., https://www.roc.noaa.gov/WSR88D/PublicDocs/NewTechnology/MESO-SAILS_Description_Briefing_Jan_2014.pdf.

Coffer, B. E., and M. D. Parker, 2017: Simulated supercells in nontornadic and tornadic VORTEX2 environments. *Mon. Wea. Rev.*, **145**, 149–180, https://doi.org/10.1175/MWR-D-16-0226.1.

——, and ——, 2018: Is there a "tipping point" between simulated nontornadic and tornadic supercells in VORTEX2 environments? *Mon. Wea. Rev.*, **146**, 2667–2693, https://doi.org/10.1175/MWR-D-18-0050.1.

——, ——, J. M. L. Dahl, L. J. Wicker, and A. J. Clark, 2017: Volatility of tornadogenesis: An ensemble of simulated nontornadic and tornadic supercells in VORTEX2 environments. *Mon. Wea. Rev.*, **145**, 4605–4625, https://doi.org/10.1175/MWR-D-17-0152.1.

Crowe, C. C., C. J. Schultz, M. Kumjian, L. D. Carey, and W. A. Petersen, 2012: Use of dual-polarization signatures in diagnosing tornadic potential. *Electron. J. Operational Meteor.*, **13**, 57–78.

Davies-Jones, R. P., and H. Brooks, 1993: Mesocyclogenesis from a theoretical perspective. *The Tornado: Its Structure, Dynamics, Prediction, and Hazards, Geophys. Monogr.*, Vol. 79, Amer. Geophys. Union, 105–114.

Dawson, D. T. II, E. R. Mansell, Y. Jung, L. J. Wicker, M. R. Kumjian, and M. Xue, 2013: Comparisons of numerically simulated and observed low-level polarimetric signatures in supercells. *36th Conf. on Radar Meteorology*, Breckenridge, CO, Amer. Meteor. Soc., 12B.6, https://ams.confex.com/ams/36Radar/webprogram/Paper229115.html.

Edwards, R., J. G. LaDue, J. T. Ferree, K. Scharfenberg, C. Maier, and W. L. Coulbourne, 2013: Tornado intensity estimation: Past, present, and future. *Bull. Amer. Meteor. Soc.*, **94**, 641–653, https://doi.org/10.1175/BAMS-D-11-00006.1.

French, M. M., and D. M. Kingfield, 2019: Dissipation characteristics of tornadic vortex signatures associated with long-duration tornadoes. *J. Appl. Meteor. Climatol.*, **58**, 317–339, https://doi.org/10.1175/JAMC-D-18-0187.1.

——, W. Burgess, E. R. Mansell, and L. J. Wicker, 2015: Bulk hook echo raindrop sizes retrieved using mobile, polarimetric Doppler radar observations. *J. Appl. Meteor. Climatol.*, **54**, 423–450, https://doi.org/10.1175/JAMC-D-14-0171.1.

Friedrich, K., E. A. Kalina, F. J. Masters, and C. R. Lopez, 2013: Drop-size distributions in thunderstorms measured by optical disdrometers during VORTEX2. *Mon. Wea. Rev.*, **141**, 1182–1203, https://doi.org/10.1175/MWR-D-12-00116.1.

Grzych, M. L., B. D. Lee, and C. A. Finley, 2007: Thermodynamic analysis of supercell rear-flank downdrafts from Project ANSWERS. *Mon. Wea. Rev.*, **135**, 240–246, https://doi.org/10.1175/MWR3288.1.

Homeyer, C. R., T. N. Sandmæl, C. K. Potvin, and A. M. Murphy, 2020: Distinguishing characteristics of tornadic and nontornadic supercell storms from composite mean analyses of radar observations. *Mon. Wea. Rev.*, **148**, 5015–5040, https://doi.org/10.1175/MWR-D-20-0136.1.

Jensen, B., T. P. Marshall, M. A. Mabey, and E. N. Rasmussen, 1983: Storm scale structure of the Pampa storm. Preprints, *13th Conf. on Severe Local Storms*, Tulsa, OK, Amer. Meteor. Soc., 85–88.

Kalina, E. A., K. Friedrich, S. M. Ellis, and D. W. Burgess, 2014: Comparison of disdrometer and X-band mobile radar observations in convective precipitation. *Mon. Wea. Rev.*, **142**, 2414–2435, https://doi.org/10.1175/MWR-D-14-00039.1.

Klees, A. M., Y. P. Richardson, P. M. Markowski, C. Weiss, J. M. Wurman, and K. K. Kosiba, 2016: Comparison of the tornadic and nontornadic supercells intercepted by VORTEX2 on 10 June 2010. *Mon. Wea. Rev.*, **144**, 3201–3231, https://doi.org/10.1175/MWR-D-15-0345.1.

Kumjian, M. R., 2011: Precipitation properties of supercell hook echoes. *Electron. J. Severe Storms Meteor.*, **6**(5), http://ejssm.org/ojs/index.php/ejssm/article/viewArticle/93.

——, and A. V. Ryzhkov, 2008: Microphysical differences between tornadic and nontornadic supercell rear-flank downdrafts revealed by dual-polarization radar measurements. *24th Conf. on Severe Local Storms*, Savannah, GA, Amer. Meteor. Soc., 3B.4, https://ams.confex.com/ams/pdfpapers/141912.pdf.

——, and ——, 2010: The impact of evaporation on polarimetric characteristics of rain: Theoretical model and practical implications. *J. Appl. Meteor. Climatol.*, **49**, 1247–1267, https://doi.org/10.1175/2010JAMC2243.1.

——, Z. J. Lebo, and H. C. Morrison, 2015: On the mechanisms of rain formation in an idealized supercell storm. *Mon. Wea. Rev.*, **143**, 2754–2773, https://doi.org/10.1175/MWR-D-14-00402.1.

Lakshmanan, V., T. Smith, G. Stumpf, and K. Hondl, 2007: The Warning Decision Support System–Integrated Information. *Wea. Forecasting*, **22**, 596–612, https://doi.org/10.1175/WAF1009.1.

Lemon, L. R., and C. A. Doswell III, 1979: Severe thunderstorm evolution and mesocyclone structure as related to tornadogenesis. *Mon. Wea. Rev.*, **107**, 1184–1197, https://doi.org/10.1175/1520-0493(1979)107<1184:STEAMS>2.0.CO;2.

Li, X., and R. C. Srivastava, 2001: An analytical solution for raindrop evaporation and its application to radar rainfall measurements. *J. Appl. Meteor.*, **40**, 1607–1616, https://doi.org/10.1175/1520-0450(2001)040<1607:AASFRE>2.0.CO;2.

Loeffler, S. D., and M. R. Kumjian, 2020: Idealized model simulations to determine impacts of storm-relative winds on differential reflectivity and specific differential phase fields. *J. Geophys. Res. Atmos.*, **125**, e2020JD033870, https://doi.org/10.1029/2020JD033870.

——, ——, M. Jurewicz, and M. M. French, 2020: Differentiating between tornadic and nontornadic supercells using polarimetric radar signatures of hydrometeor size sorting. *Geophys. Res. Lett.*, **47**, e2020GL088242, https://doi.org/10.1029/2020GL088242.

Mahalik, M. C., B. R. Smith, K. L. Elmore, D. M. Kingfield, K. L. Ortega, and T. M. Smith, 2019: Estimates of gradients in radar moments using a linear least squares derivative technique. *Wea. Forecasting*, **34**, 415–434, https://doi.org/10.1175/WAF-D-18-0095.1.

Mann, H. B., and D. R. Whitney, 1947: On a test of whether one of two random variables is stochastically larger than the other. *Ann. Math. Stat.*, **18**, 50–60, https://doi.org/10.1214/aoms/1177730491.

Markowski, P. M., 2002: Hook echoes and rear-flank downdrafts: A review. *Mon. Wea. Rev.*, **130**, 852–876, https://doi.org/10.1175/1520-0493(2002)130<0852:HEARFD>2.0.CO;2.

——, and Y. P. Richardson, 2009: Tornadogenesis: Our current understanding, forecasting considerations, and questions to guide future research. *Atmos. Res.*, **93**, 3–10, https://doi.org/10.1016/j.atmosres.2008.09.015.

——, and ——, 2014: The influence of environmental low-level shear and cold pools on tornadogenesis: Insights from idealized simulations. *J. Atmos. Sci.*, **71**, 243–275, https://doi.org/10.1175/JAS-D-13-0159.1.

——, and ——, 2017: Large sensitivity of near-surface vertical vorticity development to heat sink location in idealized simulations of supercell-like storms. *J. Atmos. Sci.*, **74**, 1095–1104, https://doi.org/10.1175/JAS-D-16-0372.1.

——, J. M. Straka, and E. N. Rasmussen, 2002: Direct surface thermodynamic observations within the rear-flank downdrafts of nontornadic and tornadic supercells. *Mon. Wea. Rev.*, **130**, 1692–1721, https://doi.org/10.1175/1520-0493(2002)130<1692:DSTOWT>2.0.CO;2.

——, Y. Richardson, M. Majcen, J. Marquis, and J. Wurman, 2011: Characteristics of the wind field in three nontornadic low-level mesocyclones observed by the Doppler on Wheels radars. *Electron. J. Severe Storms Meteor.*, **6**(3), https://www.ejssm.org/ojs/index.php/ejssm/article/viewArticle/75.

——, and Coauthors, 2012: The pretornadic phase of the Goshen County, Wyoming, supercell of 5 June 2009 intercepted by VORTEX2. Part I: Evolution of kinematic and surface thermodynamic fields. *Mon. Wea. Rev.*, **140**, 2887–2915, https://doi.org/10.1175/MWR-D-11-00336.1.

Murdzek, S. S., P. M. Markowski, and Y. P. Richardson, 2020: Simultaneous dual-Doppler and mobile mesonet observations of streamwise vorticity currents in three supercells. *Mon. Wea. Rev.*, **148**, 4859–4874, https://doi.org/10.1175/MWR-D-20-0239.1.

Orf, L., R. Wilhelmson, B. Lee, C. Finley, and A. Houston, 2017: Evolution of a long-track violent tornado within a simulated supercell. *Bull. Amer. Meteor. Soc.*, **98**, 45–68, https://doi.org/10.1175/BAMS-D-15-00073.1.

Parker, M. D., 2014: Composite VORTEX2 supercell environments from near-storm soundings. *Mon. Wea. Rev.*, **142**, 508–529, https://doi.org/10.1175/MWR-D-13-00167.1.

Pratt, J., 1959: Remarks on zeros and ties in the Wilcoxon signed rank procedures. *J. Amer. Stat. Assoc.*, **54**, 655–667, https://doi.org/10.1080/01621459.1959.10501526.

Rasmussen, E. N., and D. O. Blanchard, 1998: A baseline climatology of sounding-derived supercell and tornado forecast parameters. *Wea. Forecasting*, **13**, 1148–1164, https://doi.org/10.1175/1520-0434(1998)013<1148:ABCOSD>2.0.CO;2.

——, J. M. Straka, M. S. Gilmore, and R. Davies-Jones, 2006: A preliminary survey of rear-flank descending reflectivity cores in supercell storms. *Wea. Forecasting*, **21**, 923–938, https://doi.org/10.1175/WAF962.1.

Richardson, L. M., W. D. Zittel, R. R. Lee, V. M. Melnikov, R. L. Ice, and J. G. Cunningham, 2017: Bragg scatter detection by the WSR-88D. Part II: Assessment of Z_{DR} bias estimation. *J. Atmos. Oceanic Technol.*, **34**, 479–493, https://doi.org/10.1175/JTECH-D-16-0031.1.

Schuur, T. J., A. V. Ryzhkov, D. S. Zrnić, and M. Schönhuber, 2001: Drop size distributions measured by a 2D video disdrometer: Comparison with dual-polarization radar data. *J. Appl. Meteor.*, **40**, 1019–1034, https://doi.org/10.1175/1520-0450(2001)040<1019:DSDMBA>2.0.CO;2.

Shabbott, C. J., and P. M. Markowski, 2006: Surface in situ observations within the outflow of forward-flank downdrafts of supercell thunderstorms. *Mon. Wea. Rev.*, **134**, 1422–1441, https://doi.org/10.1175/MWR3131.1.

Smith, B. T., R. L. Thompson, J. S. Grams, C. Broyles, and H. E. Brooks, 2012: Convective modes for significant severe thunderstorms in the contiguous United States. Part I: Storm classification and climatology. *Wea. Forecasting*, **27**, 1114–1135, https://doi.org/10.1175/WAF-D-11-00115.1.

Stensrud, D. J., J. V. Cortinas Jr., and H. E. Brooks, 1997: Discriminating between tornadic and nontornadic thunderstorms using mesoscale model output. *Wea. Forecasting*, **12**, 613–632, https://doi.org/10.1175/1520-0434(1997)012<0613:DBTANT>2.0.CO;2.

Van Den Broeke, M. S., 2020: A preliminary polarimetric radar comparison of pretornadic and nontornadic supercell storms. *Mon. Wea. Rev.*, **148**, 1567–1584, https://doi.org/10.1175/MWR-D-19-0296.1.

Weiss, C. C., D. C. Dowell, J. L. Schroeder, P. S. Skinner, A. E. Reinhart, P. M. Markowski, and Y. P. Richardson, 2015: A comparison of near-surface buoyancy and baroclinity across three VORTEX2 supercell intercepts. *Mon. Wea. Rev.*, **143**, 2736–2753, https://doi.org/10.1175/MWR-D-14-00307.1.

Wilcoxon, F., 1945: Individual comparisons by ranking methods. *Biom. Bull.*, **1**, 80–83, https://doi.org/10.2307/3001968.

Wurman, J., D. Dowell, Y. Richardson, P. Markowski, E. Rasmussen, D. Burgess, L. Wicker, and H. B. Bluestein, 2012: The Second Verification of the Origins of Rotation in Tornadoes Experiment: VORTEX2. *Bull. Amer. Meteor. Soc.*, **93**, 1147–1170, https://doi.org/10.1175/BAMS-D-11-00010.1.